ADVANCED FUNCTIONAL MATERIALS
www.afm-journal.de

Self-Assembly of Mechanoplasmonic Bacterial Cellulose–Metal Nanoparticle Composites

*Olof Eskilson, Stefan B. Lindström, Borja Sepulveda, Mohammad M. Shahjamali, Pau Güell-Grau, Petter Sivlér, Mårten Skog, Christopher Aronsson, Emma M. Björk, Niklas Nyberg, Hazem Khalaf, Torbjörn Bengtsson, Jeemol James, Marica B. Ericson, Erik Martinsson, Robert Selegård, and Daniel Aili**

Nanocomposites of metal nanoparticles (NPs) and bacterial nanocellulose (BC) enable fabrication of soft and biocompatible materials for optical, catalytic, electronic, and biomedical applications. Current BC–NP nanocomposites are typically prepared by in situ synthesis of the NPs or electrostatic adsorption of surface functionalized NPs, which limits possibilities to control and tune NP size, shape, concentration, and surface chemistry and influences the properties and performance of the materials. Here a self-assembly strategy is described for fabrication of complex and well-defined BC–NP composites using colloidal gold and silver NPs of different sizes, shapes, and concentrations. The self-assembly process results in nanocomposites with distinct biophysical and optical properties. In addition to antibacterial materials and materials with excellent senor performance, materials with unique mechanoplasmonic properties are developed. The homogenous incorporation of plasmonic gold NPs in the BC enables extensive modulation of the optical properties by mechanical stimuli. Compression gives rise to near-field coupling between adsorbed NPs, resulting in tunable spectral variations and enhanced broadband absorption that amplify both nonlinear optical and thermoplasmonic effects and enables novel biosensing strategies.

1. Introduction

Templated synthesis or deposition of metal nanoparticles (NPs) in nanocellulose can enable development of cellulose-based nanocomposites with novel optical,[1,2] electronic,[3,4] catalytic,[5,6] and biophysical properties.[7,8] Nanocellulose can be derived from plant sources but can also be produced by bacteria.[9] Bacterial nanocellulose (BC) is an exopolysaccharide chemically identical to plant cellulose, produced and secreted by aerobic Gram-negative bacteria, such as *Komagataeibacter xylinus* (formerly *Gluconacetobacter xylinus*).[10,11] BC forms highly hydrated and entangled 3D networks of well-defined nanocellulose fibrils that are about 40 to 60 nm in diameter, 1 to 10 µm in length and a degree of crystallinity reaching 90%.[12] In contrast to plant-derived cellulose, BC is not contaminated with lignin and hemicellulose[13,14] and can be utilized to

O. Eskilson, Dr. M. M. Shahjamali, P. Sivlér, M. Skog, Dr. C. Aronsson, N. Nyberg, Dr. E. Martinsson, Dr. R. Selegård, Prof. D. Aili
Laboratory of Molecular Materials
Division of Biophysics and Bioengineering
Department of Physics,
Chemistry and Biology (IFM)
Linköping University
Linköping SE-581 83, Sweden
E-mail: daniel.aili@liu.se

Prof. S. B. Lindström
Division of Solid Mechanics
Department of Management and Engineering (IEI)
Linköping University
Linköping SE-581 83, Sweden

Dr. B. Sepulveda
Catalan Institute of Nanoscience and Nanotechnology (ICN2)
CSIC and BIST
Campus UAB, Bellaterra, Barcelona 08193, Spain

The ORCID identification number(s) for the author(s) of this article can be found under https://doi.org/10.1002/adfm.202004766.

DOI: 10.1002/adfm.202004766

Dr. M. M. Shahjamali
School of Engineering and Applied Sciences
Harvard University
9 Oxford Street, Cambridge, MA 02138, USA

P. Güell-Grau
Instituto de Microelectrónica de Barcelona (IMB-CNM, CSIC)
Campus UAB, Bellaterra, Barcelona 08193, Spain

Dr. E. M. Björk
Nanostructured Materials
Department of Physics,
Chemistry and Biology (IFM)
Linköping University
Linköping SE-58183, Sweden

Dr. H. Khalaf, Prof. T. Bengtsson
Cardiovascular Research Centre
School of Medical Sciences
Örebro University
Örebro SE-70362, Sweden

J. James, Prof. M. B. Ericson
Biomedical Photonics Group
Department of Chemistry and Molecular biology
University of Gothenburg
Gothenburg SE-412 96, Sweden

produce pure nanocellulose membranes with high mechanical strength, large water-holding capacity and large specific surface area.[9] In addition, BC is nontoxic, biodegradable, and inert to human metabolism and demonstrates excellent biocompatibility.[15] BC is thus an attractive and versatile material for a wide range of applications and has, among others, been utilized as a scaffold for tissue engineering[16,13] and as a soft substrate for biosensors[2] and bioelectronics.[17] BC is also a material of great interest for wound care applications and BC-based wound dressings have shown promising results in the clinic for treatment of burns and nonhealing wounds.[18,19]

Gold (AuNP) and silver (AgNP) nanoparticles demonstrate unique optical, antibacterial, and catalytic properties, and a large number of methods have been developed for templated in situ synthesis of these NPs in BC for fabrication of functional materials.[2,20] The porous structure of the fibrillar BC network enables diffusion of metal ions and reducing agents into the material where the ether oxygen and hydroxyl groups of cellulose can sequester the ions and stabilize the resulting metal NPs.[21] Although the cellulose can also contribute to the reduction of the metal ions,[2,22] reducing agents such as borhydride, hydrazine, hydroxylamine, ascorbic acid,[23] and triethanolamine[24] are widely used, as well as microwave[25] and UV-radiation.[26] In order to prevent NP aggregation after synthesis, various polymers can be added to stabilize the NPs.[23] Possibilities to chemically modify the BC with a reducing agent, such as amidoxime,[6] or by adsorption of poly(ethyleneimine)[22] have also been explored. Modifying the BC or adding reducing agents or other reagents can influence the mechanical, structural, and chemical properties of the BC.[26] In situ synthesis also occurs under conditions that are difficult to control and there are many aspects relating to the BC that can influence the outcome of the synthesis, including presence of unknown contaminating species remaining from the fermentation process.[27] Consequently, there are limited possibilities to control NP properties, distribution, and concentration.[6] Preparation of composites comprising multiple types of nanoparticles can also be challenging since the sequential addition of different metal salts and reducing agents would likely result in nanoparticles that are undefined with respect to size and composition.[28]

In contrast, a large number of strategies for solution-based synthesis of high-quality colloidal metal NPs have been developed and optimized to yield NPs of defined sizes,[29] shapes,[30,31] and compositions[32] and with narrow size distributions.[33] The possibility to use presynthesized colloidal NPs in the fabrication of BC-based nanocomposites can potentially enable fabrication of more well-defined and complex materials with a wider range of optical and biophysical properties.[34] To this end, composites of BC aerogels and presynthesized gold nanorods (AuNRs) and spherical gold NPs (AuNPs) have been generated by immersing freeze-dried BC in concentrated suspensions of presynthesized colloidal NPs coated with cationic surfactants (cetyl trimethylammonium bromide (CTAB))[1] and cationic thiols (4,6-diamino-2-pyrimidinethiol),[35] respectively. Because of the capillary effects, the NPs were efficiently taken up in the BC aerogel network and were retained by electrostatic interactions between the NPs and the BC. In addition to the need of drying the BC and the cytotoxicity of CTAB,[36] the presence of surfactants or thiol monolayers complicates further surface functionalization of the NPs, which reduces the versatility of the materials.

Herein, we describe a generic self-assembly strategy for tunable functionalization of hydrated BC membranes with presynthesized colloidal NPs (**Figure 1**a), that facilitates development of advanced BC-based nanocomposite materials. The self-assembly process was optimized to proceed under ambient conditions for both citrate- and surfactant-stabilized NPs of different shapes and compositions. The interactions involved was investigated in detail and the resulting nanocomposite materials could be tailored to demonstrate antimicrobial properties, excellent refractive index sensing performance, and enhanced thermoplasmonic and nonlinear optical effects. In addition, the homogenous incorporation of AuNPs in the BC allowed for modulation of the plasmonic near-field coupling in three dimensions by mechanical deformation of the BC membranes. By compressing the hydrated BC–AuNP nanocomposites, the decrease in separation between the adsorbed NPs resulted in plasmonic near-field coupling. The induced optical shifts and peak broadening can be directly correlated to the mechanical pressure and give rise to both amplified nonlinear optical effects and enhanced thermoplasmonic heating. Moreover, adsorption of proteins on the AuNPs introduces a steric barrier that reduces the magnitude of the spectral changes, which enables a novel optical biosensing readout strategy using mechanical stimuli. This versatile strategy for functionalization of BC with metal NPs can facilitate fabrication of multifunctional soft nanomaterials for a wide range of optical and biomedical applications, including biosensing and advanced wound care.

2. Results and Discussion

2.1. Nanoparticle Self-Assembly

Native BC is a nanofibrillar and translucent material (Figure 1b) with a porosity that typically exceeds 0.90,[37] which enables diffusion of NPs and macromolecules into the material, although with a reduced diffusivity. Noninteracting macromolecules (dextran, 44–260 kDa) have been shown to experience a hindrance ratio of about 0.4 compared to the theoretical maximum diffusion rate.[37] When immersed in an aqueous suspension of citrate-stabilized gold NPs (AuNPs) in the presence of moderate NaCl concentrations ($\approx 5 \times 10^{-3}$ M), we observed that hydrated BC membranes over time adopted a pink hue, indicating that AuNPs were adsorbing in the material. The concentration of NPs in the membrane continued to increase until nearly all the AuNPs in the suspension had adsorbed in the BC, resulting in a bright red membrane (Figure 1c and Figure S1, Supporting Information) with a well-defined localized surface plasmon resonance (LSPR) band (Figure 1d) and an extinction maximum (λ_{max}) at about 533 and 520 nm for AuNPs with a diameter of 50 and 13 nm, respectively. The adsorption process follows pseudo-first-order kinetics with a rate constant of 0.013 s^{-1} for 50 nm AuNPs (Figure 1e). After 14 d of incubation, about 90% of all the particles in the suspension (75×10^{-12} M) were adsorbed in the membrane. This corresponds to a concentration of 5×10^{-9} M confined in the BC membrane. A similar trend with respect to the adsorption kinetics was also seen for 13 nm AuNPs,

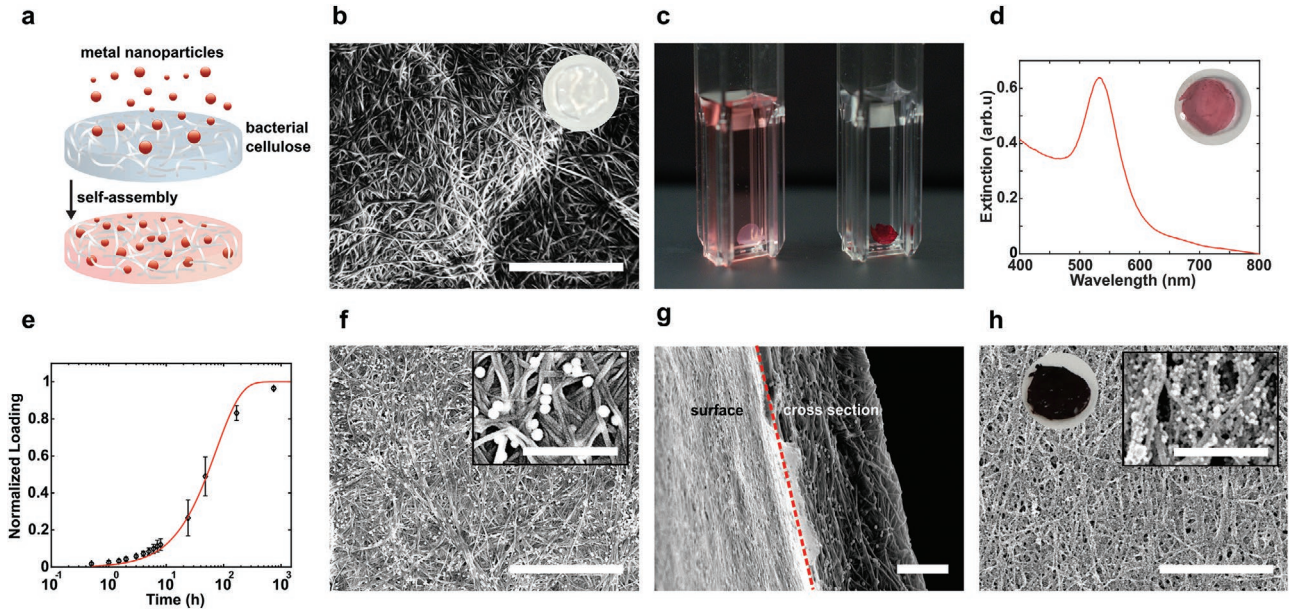

Figure 1. a) Gold nanoparticles (AuNPs) were adsorbed in bacterial cellulose (BC) membranes to generate soft nanoplasmonic materials. b) SEM micrograph and photograph (inset) of native BC, scale bar: 3 µm. c) BC membranes (bottom of the cuvette) were immersed in aqueous suspensions of 50 nm AuNPs (left) and the adsorption of the AuNPs to the BC resulted in complete depletion of the AuNPs in suspension (right). d) Extinction spectrum and photo of an BC–AuNP composite membrane (ø 6 mm) prepared using 60×10^{-12} M 50 nm AuNP and 120 h incubation. e) Adsorption kinetics of 50 nm AuNPs (75×10^{-12} M) to BC membranes, 5×10^{-3} M NaCl, $n \geq 3$, normalized loading is defined as the concentration of AuNP in BC normalized with respect to the initial AuNP concentration in suspension. Error bars show standard deviations. f) SEM of BC–AuNP composite after 120 h incubation and 75×10^{-12} M 50 nm AuNPs, scale bar: 3 µm, scale bar inset: 500 nm. g) SEM of a BC cross-section indicating homogenous adsorption of AuNPs in the BC, scale bar: 1 µm. h) SEM and photo (inset, left) of BC–AuNP composite (ø 6 mm) prepared using concentrated 13 nm AuNP suspension (14.6×10^{-9} M) and 14 d incubation, scale bar: 3 µm, scale bar inset: 500 nm.

showing a rate constant of $k = 0.008$ s^{-1} (Figure S2, Supporting Information). Interestingly, for both sizes of NPs essentially all available AuNPs were adsorbed in the BC membranes, resulting in an almost complete depletion of the AuNPs from the suspension (Figure 1c). Since the adsorption process was diffusion limited, increasing nanoparticle concentration and applying gentle agitation significantly increased the rate of adsorption. The composites used in subsequent experiments were prepared by incubating BC for about 12 h under conditions optimizing the adsorption rate, as detailed in the experimental section.

Scanning electron microscopy (SEM) images of the BC–AuNP composites show that the NPs were homogenously distributed in the membranes and also diffused into the interior of the BC membranes (Figure 1f,g and Figure S3, Supporting Information). The SEM micrographs also indicate that the AuNPs adsorb to the nanocellulose fibrils rather than being physically trapped in the pores. This was further confirmed by the slight redshift of the LSPR band ($\Delta\lambda_{max} \approx 1$ nm) of the AuNPs after adsorption in the BC (Figure S4, Supporting Information). The scattering of the BC blueshifts the LSPR band by about 1 nm and the shift due to the substrate effect was consequently about 2 nm, which is similar to AuNPs immobilized on 2D polymer substrates.[38,39] This small shift cannot be distinguished by eye and the perceived color of the membranes were hence very similar to that of the original suspension. Although a certain amount of lateral aggregation can be seen in the SEM micrographs, this is likely an effect of drying since the wet AuNP-functionalized BC membranes display a well-defined LPSR band (Figure 1d). Aggregation results in a larger redshift (>10 nm) and broadening of the LSPR band due to plasmonic coupling,[40] which was not seen here. The specific surface area of the BC was about 75 m^2 g^{-1} as determined using nitrogen adsorption (Figure S5, Supporting Information). Based on the average dry mass of the BC membranes (0.36 ± 0.05 mg, ø 6 mm), the surface concentration of AuNPs on the fibrils is estimated to 1.3×10^{12} m^{-2} after 120 h incubation with 50 nm AuNP at an initial concentration of 60×10^{-12} M, which correspond to a surface coverage of about 0.3% if assuming a homogenous distribution of AuNPs within the membranes. Hence, large amounts of AuNPs can be adsorbed in the membranes without any risk of substantial plasmonic coupling due to crowding. To investigate whether the amount of adsorbed AuNPs could be further increased, BC membranes were incubated in a more concentrated suspension of 13 nm diameter AuNPs (14.6×10^{-9} M). After 14 d of incubation the AuNPs completely covered the fibrils (Figure 1h). Because of the small separation between the AuNPs and the resulting near-field interactions, the BC membranes show limited transmission in the visible wavelength range and appear completely opaque (Figure 1h inset and Figure S6, Supporting Information).

2.2. Modeling of Interactions

The AuNPs were strongly bound to the BC and only minor release, corresponding to less than 10% of the total amount of

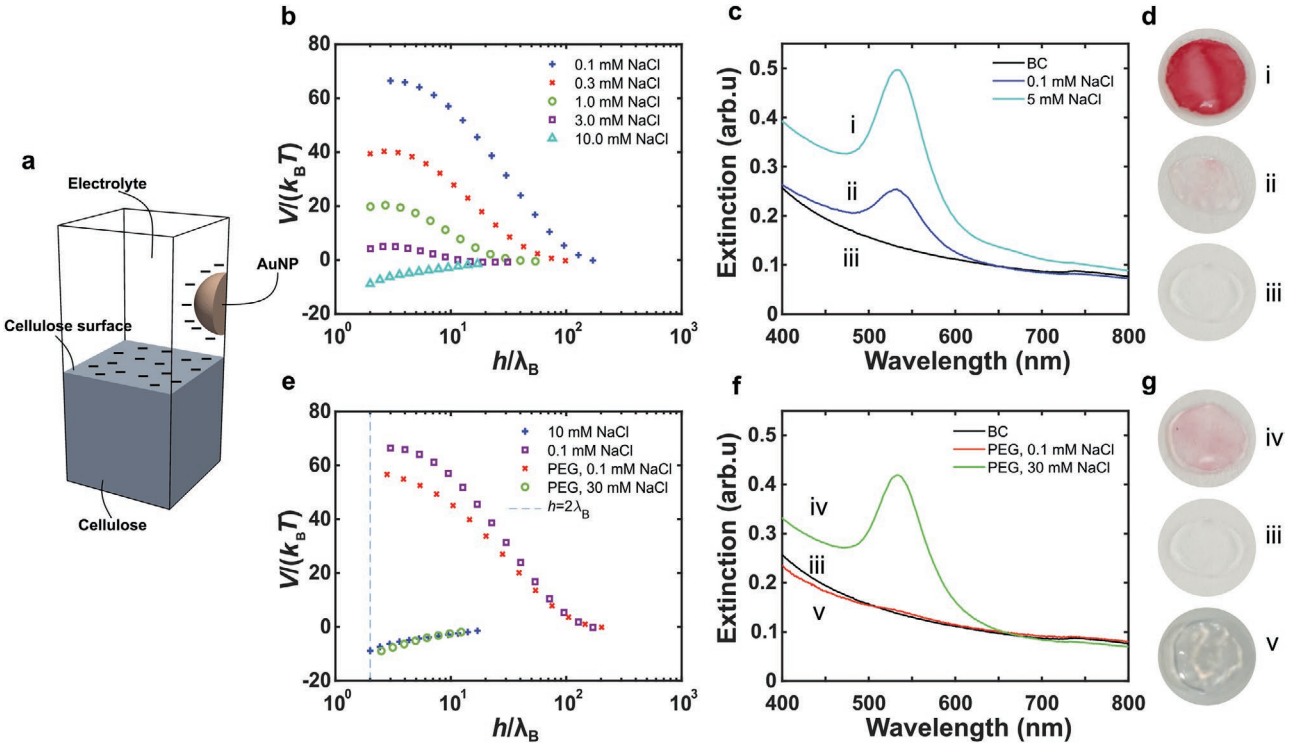

Figure 2. a) The potential of mean force $V(h)$ between the AuNPs and the BC was modeled by solving the Poisson–Boltzmann equation for a gold sphere interacting with a flat cellulose halfspace in a monovalent electrolyte. b) Simulation of interaction potential as a function of separation (h) between the AuNPs and the BC normalized by the Bjerrum length (λ_B) in presence of 0.1×10^{-3}–10×10^{-3} M NaCl. c) UV–vis data and d) corresponding photographs showing the increase in AuNP adsorption with increasing concentration of NaCl. e) Simulation of the influence of PEG and NaCl concentration on the interaction potential and f) corresponding experimental UV–vis and g) photographs showing increased adsorption of PEG functionalized AuNPs with increasing NaCl concentration.

AuNPs adsorbed in the BC, was observed even after extensive washing in water or ethanol for 7 d (Figure S7a, Supporting Information). Moreover, only minor effects were observed when the BC–AuNP composites were exposed to buffers with pH values ranging from 3 to 7.0, whereas at pH 8.5 some aggregation occurred (Figure S8, Supporting Information). To further understand the cause of this apparently strong interaction between the AuNPs and the BC, the potential of mean force $V(h)$ was modeled, where h is the separation between the AuNP and BC surfaces (**Figure 2**a and Figure S9, Supporting Information). The separation was normalized using the Bjerrum length $\lambda_B \approx 0.7$ nm in water at room temperature (RT). The Poisson–Boltzmann equation was solved for a gold sphere interacting with a flat cellulose half-space in a monovalent electrolyte (for details, see Supporting Information). Forces originating from van der Waals interactions, osmotic pressure and electrostatic Maxwell stress were taken into account. In a range of low ionic strength, electrostatic repulsion caused by double-layer interactions of like-charged surfaces creates a potential barrier $\Delta V = \max_h V(h)$. Since the rate of adsorption is proportional to $\exp(-\Delta V/k_B T)$,[41,42] where k_B is the Boltzmann constant and T is the absolute temperature, this potential barrier essentially prevents adsorption of AuNPs onto the BC fibrils, which stabilizes the system. However, as the ionic strength increases, the thicknesses of the electric double-layers decrease, thus reducing the repulsive electrostatic interaction as quantified by ΔV (Figure 2b). At a sufficiently high salt concentration, ΔV is reduced to the point where the AuNP adsorption process occurs on experimental time scales through an activated process. Under these conditions, the AuNPs can come into physical contact with the BC, where short-range van der Waals attraction dominates the adsorption process. These findings were experimentally confirmed by monitoring the adsorption of AuNPs to BC in the presence of 0.1×10^{-3} or 5×10^{-3} M NaCl (Figure 2c,d), where the latter condition resulted in a drastically larger amount of adsorbed AuNPs. Due to the limited colloidal stability of citrate-stabilized NPs, higher concentrations of NaCl led to NP aggregation and could not be used. Hence, optimizing conditions for the adsorption process involves balancing colloidal stability and the thickness of the electric double layer by moderating the ionic strength of the solution.

In an attempt to modify the short-range attraction between AuNPs and BC, the AuNPs were functionalized with carboxyl-terminated polyethylene glycol (PEG) disulfide with a molecular weight of 2.9 kDa. PEG-functionalization resulted in an LSPR shift of $\Delta\lambda_{max} = 2.4$ nm and an increase in hydrodynamic radius (R_H) from about 24.3 to about 27.4 nm ($\Delta R_H = 3.1$ nm), as well as a moderate change in zeta potential (ζ) from –66 to –48 mV, confirming formation of a self-assembled monolayer of the PEG on the AuNPs. Despite the less negative zeta potential, the PEG-functionalization completely prevented adsorption of the AuNPs to BC at low salt concentrations (0.1×10^{-3} M NaCl).

However, the presence of PEG improved the colloidal stability of the AuNPs and effects of higher ionic strengths could be explored. Increasing the NaCl concentration to 30×10^{-3} M NaCl resulted in a decrease in hydrodynamic radius to 24.6 nm, likely due a compression of both the PEG layer and the electric double layer, but the particles remained dispersed. Interestingly, at this ionic strength, the PEG–AuNPs clearly adsorbed to the BC (Figure 2f,g), albeit to a slightly lower extent than the non-functionalized AuNPs at 5×10^{-3} M NaCl. These findings were further confirmed by modeling. The adsorbed PEG layer was modeled as a spherical dielectric shell on the AuNPs with the same properties as water with the charged groups of the polymer located on the outer surface of this shell. The thickness of the shell was taken as the difference between the hydrodynamic radius of functionalized and nonfunctionalized AuNPs. The simulated potential of mean force was not much affected by the presence of the polymeric brush, and at high ionic strength the polymers appears not to provide sufficient steric repulsion to prevent adsorption (Figure 2e).

2.3. Self-Assembly of BC–AgNP, BC–AgNP/AuNP, and BC–AuNR Composites

The strategy developed for the self-assembly of metal NPs in hydrated BC was not restricted to spherical AuNPs. To verify the versatility of the approach, we also investigated adsorption of silver NPs (AgNPs) for generating of BC–AgNP composites and BC–AgNP/AuNP composites, as well as adsorption of various anisotropic CTAB-stabilized gold NPs, such as gold nanorods (AuNRs). BC–AgNP composites have a distinct yellow color and show a well-defined LSPR band at about λ_{max} = 400 nm (**Figure 3**a). The SEM micrographs show that the AgNPs are well-dispersed and adsorbed to the fibrils (Figure 3b). Silver-impregnated wound dressings are widely used in treatment of infected wounds and BC–AgNP composites can thus further enhance the performance of BC as a wound care material.[43] To also investigate whether this fabrication strategy result in materials with antimicrobial properties, the BC–AgNP composites were immersed in suspension of *Staphylococcus aureus* (10^7 CFU) and the bacteriolytic effect was assessed using the fluorescent nucleic acid stain Sytox Green. The native BC did not show any antibacterial effects, but the viability of the bacteria was markedly reduced in the vicinity of the BC–AgNP composite membranes (Figure 3c). Since the AgNPs appear to be as strongly bound to the BC as the AuNPs, the antibacterial effect is likely due to a gradual dissolution of the nanoparticles which generates Ag^+ ions.[44]

Whereas in situ metal NP synthesis can only yield composites with a single type of NPs, this is not a restriction when using self-assembly. We demonstrate this by incubating BC membranes in a suspension containing both AgNPs and AuNPs, resulting in a mixed BC–AgNP/AuNP composite material (Figure 3d–g). The BC–AgNP/AuNP composite membranes show two distinct LSPR bands at $\lambda_{max} \approx$ 398 nm and at $\lambda_{max} \approx$ 532 nm originating from the immobilized AgNPs and AuNPs, respectively (Figure 3d). By varying the concentration of AgNPs between 38×10^{-12} M and 0.48×10^{-9} M and the concentration of AuNPs between 17×10^{-12} and 47×10^{-12} M in the initial suspension, the ratio of adsorbed NPs could be controlled. Altering the ratio of the two types of NPs changed the relative intensities of the AgNP and AuNP LSPR bands, resulting in a transition in color of the BC membranes from yellow to red/orange (Figure 3d,e). The two types of NPs were homogenously distributed in the materials and could not be distinguished in SEM micrographs (Figure 3f) but energy-dispersive X-ray spectroscopy (EDS) confirmed the presence of both silver and gold in the composites (Figure 3e).

In addition to NP size and composition, shape is an important factor for tuning the optical properties of colloidal NPs (Figure S10, Supporting Information). Fabrication of BC composites with nonspherical anisotropic NPs can further expand the range of nanoplasmonic properties of the materials. Most anisotropic colloidal NPs, such as AuNRs, are synthesized in the presence of surfactants, most notably CTAB. The presence of CTAB can complicate both surface immobilization and functionalization,[45] and previous attempts to impregnate BC with CTAB-stabilized NPs exploited freeze-dried BC aerogels where capillary effects could accelerate the adsorption process.[1] To facilitate adsorption of CTAB-stabilized AuNRs in hydrated BC, excess CTAB was first carefully removed and the NRs were redispersed in water. In the absence of excess CTAB, AuNRs adsorbed readily in the hydrated BC membranes (Figure 3h, inset). The BC–AuNR composites show a significant broadening of the long wavelength resonance in the LSPR spectrum compared to the dispersed rods (Figure 3h and Figures S10 and S11, Supporting Information). SEM micrographs indicate that AuNRs align with the cellulose nanofibrils, resulting in formation of both parallel bundles and AuNRs arranged in a tail-to-tail orientation (Figure 3i). The ordering of the AuNRs along the cellulose nanofibrils result in defined near-field interaction between the rods. Simulations show that the tail-to-tail arrangement of the AuNRs produces a pronounced redshift whereas the formation of parallel bundles induces a blueshift of the long wavelength resonance corresponding to the long axis of the rods (Figure S10, Supporting Information), which explains the observed broadening of the LSPR band. For the short wavelength resonance, this near-field effect is much weaker for both tail-to-tail and parallel arrangements of the rods and, consequently, no shift of this plasmon band was seen. Combined, the interactions between the BC and the AuNRs result in a quasi-ordered nanocomposite with very distinct optical properties. This assembly strategy could also be extended to other anisotropic NPs, including longer AuNRs (Figure 3j and Figure S10b,e, Supporting Information) and gold nanoprisms (Figure 3j and Figure S10c,f, Supporting Information), which further indicate the extensive possibilities to produce BC–metal NP composites with tailored optical properties.

2.4. Mechanoplasmonic Properties

As indicated by the SEM cross section of the BC–AuNP (Figure 1g), the AuNPs readily diffuse into the bulk of the nanocellulose network. Since the BC membranes are highly hydrated, individual fibrils are typically well separated in the wet state. When compressing the material, the separation between

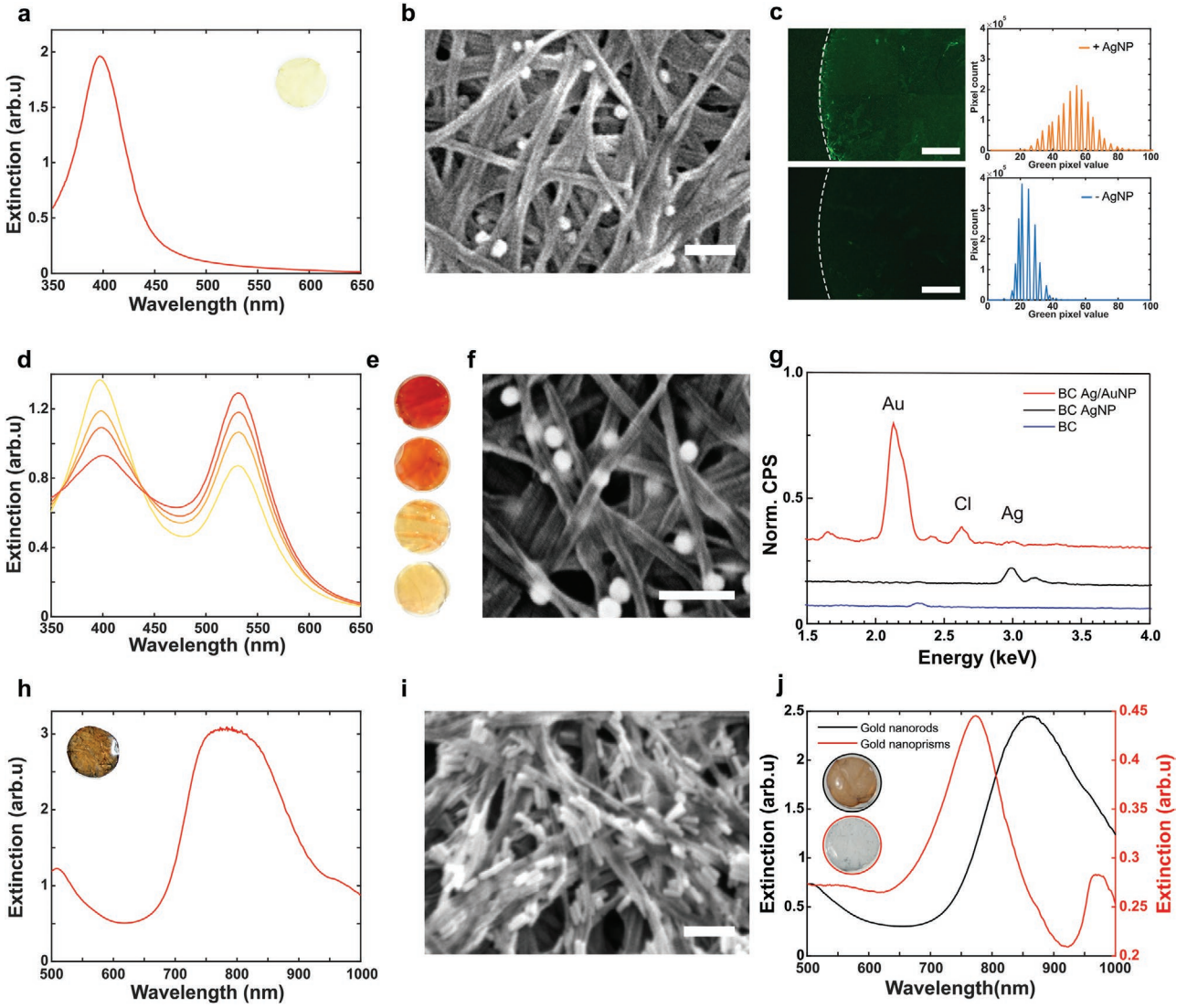

Figure 3. a) UV–vis spectrum and photo of BC–AgNPs (ø 20 nm). b) SEM of BC–AgNP membranes (ø 40 nm) incubated in 3.75×10^{-12} M AgNPs for 7 d, scale bar: 200 nm. c) Sytox Green staining of BC membranes with and without adsorbed AgNPs (ø 40 nm) immersed in *Staphylococcus aureus* (10^7 CFU) suspension, scale bar: 500 µm. d) UV–vis spectra of BC membranes incubated in a mixture of AgNP (ø 20 nm) and AuNP (ø 50 nm) suspensions with varying particle concentration ratios. e) photos of membranes incubated in different ratios of AgNPs (ø 20 nm) and AuNPs (ø 50 nm), from top to bottom [AgNP]:[AuNP]: 6:1; 10:1; 17:1; 28:1. f) SEM micrograph of BC membrane incubated in a mixture of AgNP (ø 20 nm, 25×10^{-12} M) and AuNP (ø 50 nm, 46×10^{-12} M) suspensions for 7 d, scale bar: 200 nm. g) EDX measurement of the NP functionalized BC membranes. h) UV–vis spectrum, photo, and i) SEM micrograph of AuNRs (58×13 nm) adsorbed in BC, scale bar: 200 nm. j) UV–vis spectra and photo of BC–AuNRs (50×10 nm) and gold BC-nanoprisms (70 nm).

individual fibrils will decrease, increasing the chances of near-field interactions between adsorbed AuNPs (**Figure 4**a). A similar phenomenon has been described by Park et al.,[46] where BC–AuNP composites subject to drying showed amplified surface-enhanced Raman scattering (SERS) signals due to deformation of the BC and formation of hotspot. To investigate this effect further, a defined pressure was applied on the BC–AuNP membranes using a rheometer with an optically transparent plate and a reflecting geometry. The optical response was measured in real-time using a fiber-optical spectrophotometric setup (Figure S12, Supporting Information). Interestingly, a distinct and instantaneous redshift and a pronounced broadening of the LPSR band was seen when pressure was applied (Figure 4b,c and Figure S13, Supporting Information) and that increased as a function of pressure (Figure 4d). Part of the redshift can be attributed to an increase in effective refractive index (RI) in the vicinity of the AuNPs upon compression as a result of decreasing separation between the individual nanocellulose fibrils. However, the magnitude of the LSPR shift, including the broadening of the LSPR band, clearly indicate that the compression reduces the separation between a large fraction of the immobilized AuNPs enough to give rise to plasmonic near-field coupling. The broadening, manifested as the appearance of a distinct shoulder in the wavelength range between 600 and

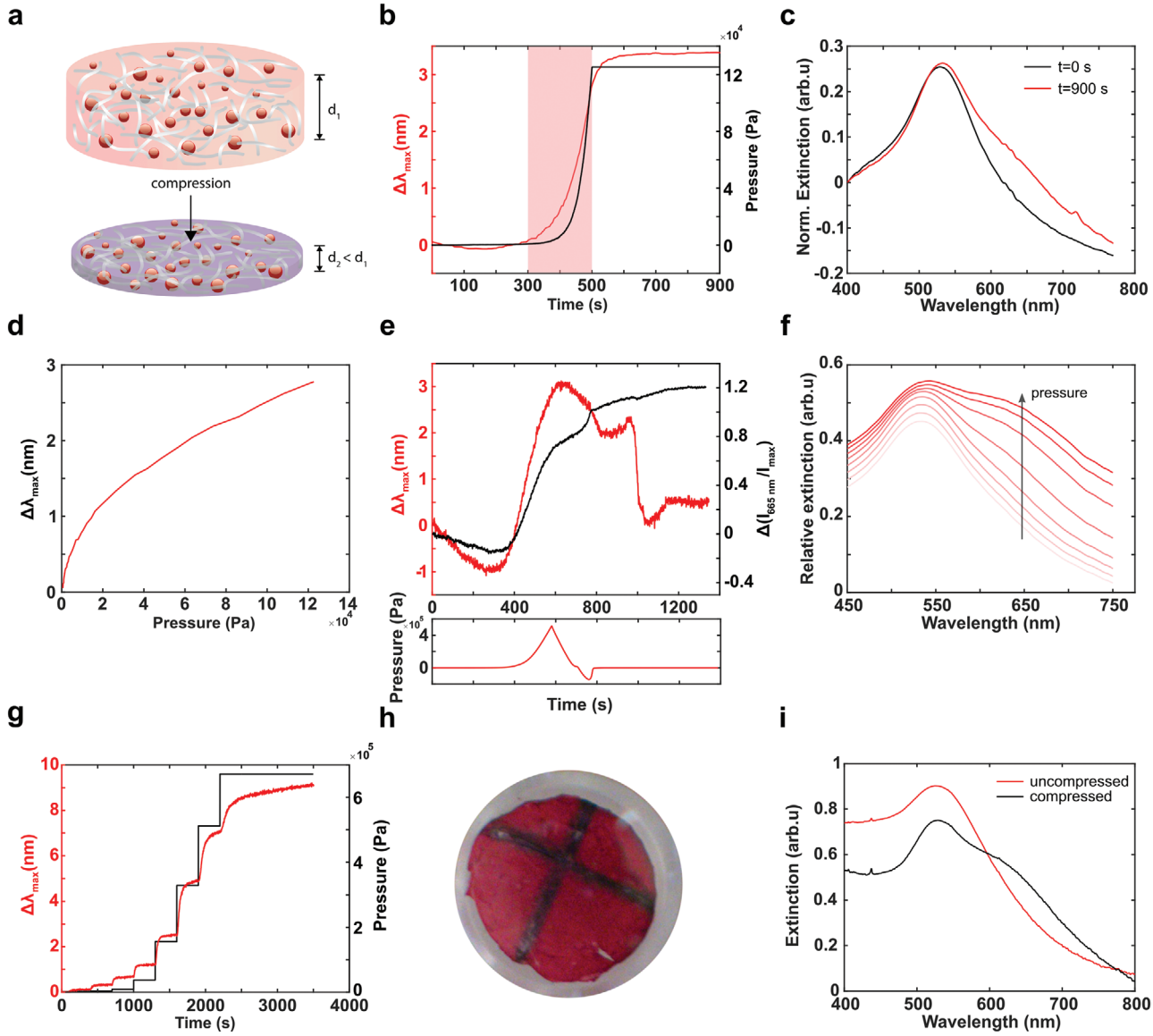

Figure 4. a) Compression of the water swollen BC–AuNP composites reduces separation between adsorbed AuNPs resulting in plasmonic coupling and a distinct redshift of the LSPR band. b) LSPR peak shift when pressure is applied to a BC–AuNP composite. c) UV–vis spectra obtained at timepoint $t = 0$ s and $t = 900$ s. d) LSPR peak shift as a function of pressure during compression in (b) indicated in red. e) Real-time LSPR peak shift and broadening of a BC–AuNP composite upon compression. f) UV–vis spectra of BC–AuNP when pressure is increased in distinct steps, and g) corresponding real-time data of the LSPR peak shift. h) Photo of BC–AuNP composites after compression in a cross-pattern, resulting in a substantial colorimetric shift in the compressed regions. The noncompressed parts of the BC–AuNP composite retained the original red color. i) UV–vis spectra obtained from the compressed and non-compressed parts of the BC–AuNP composite shown in (h).

800 nm, was quantified as the ratio of the intensity at 665 nm and the LSPR peak maximum.

BC–AuNP composites subject to moderate compression (<500 kPa) show a partial reversion of the redshift when releasing the pressure, whereas the broadening of the LSPR band was retained (Figure 4e). The blueshift of the LSPR peak position when releasing the pressure indicate a partial recovery and restoration of the local RI in the membranes. The relaxation of the BC was, however, not sufficient to separate AuNPs forced into close proximity, as indicated by the irreversible broadening of the LSPR band. The fraction of AuNPs experiencing significant near-field interactions increased with increasing pressure. A stepwise increase in the pressure consequently resulted in a concomitant stepwise redshift in the peak position and broadening of the LSPR band (Figure 4f,g). The inelastic response of the material further allows for controlling the nanoplasmonic properties with spatial resolution by applying different pressure in different parts of the composites. Pressure applied in a cross-pattern result in a spatially distinct mechanoplasmonic shift that could be clearly distinguished both spectrophotometrically and by the naked eye (Figure 4h,i). Noncompressed regions of the membrane

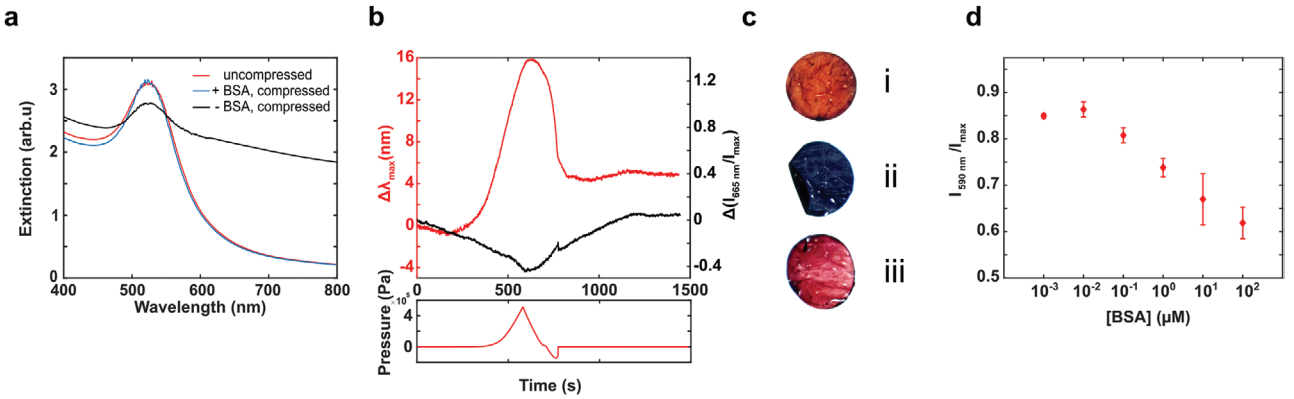

Figure 5. a) Influence of BSA adsorption (10 mg mL^{-1}) on the mechanoplasmonic response and b) real-time LSPR peak shift and broadening during compression of BC–AuNP modified with BSA. c) Corresponding photographs of BC–AuNP composite without BSA (i) before and (ii) after compression, and (iii) when incubated with BSA before compression. d) Influence of BSA concentration on the mechanoplasmonic response. Error bars show standard deviations.

remained unaffected and retained the bright red color indicative of well-separated AuNPs.

To further confirm that compression leads to an increase in the near-field electromagnetic interaction between the immobilized AuNPs, bovine serum albumin (BSA, 10 mg mL^{-1}) was adsorbed on the AuNPs prior compression. The addition of BSA resulted in a small shift in the LSPR band ($\Delta\lambda_{max}$ = 3.7 nm) indicative of adsorption of the protein on the NPs (Figure S14a, Supporting Information). Although a significant transient redshift was seen upon compression, the adsorbed BSA completely inhibited the broadening of the LSPR band (**Figure 5**a–c). Photographs of the BC–AuNP composites before and after compression highlights the distinct color change that occurs in the absence of BSA whereas the corresponding photographs of BC–AuNP composites exposed to BSA before compression show a similar color as the noncompressed composites (Figure 5c). For the latter, the perceived color can be slightly different as compared to the noncompressed samples due to the differences caused by the RI shift upon BSA-adsorption as well as the thinning of the membrane upon compression. The striking differences in the LSPR band and color between samples with and without BSA after compression, however, clearly indicate that the adsorbed BSA can provide a steric barrier that prevents close contact between the AuNPs. This drastically reduces the near-field coupling and consequently the magnitude of the optical response when compressed. The BSA-dependent mechanoplasmonic response showed a clear concentration dependence. The lower the concentration of BSA the larger the mechanoplasmonic response, with a dynamic range that spans over five orders of magnitude (Figure 5d and Figure S14d, Supporting Information). The spectral variations induced in the mechanoplasmonic response (peak position and broadening) in the presence and absence of BSA are on par with the distinct colorimetric response of aggregating AuNPs in suspension, which have been widely explored for bioanalytical applications.[47] However, since the AuNPs are adsorbed on the BC, the difficulties with controlling NP colloidal stability, especially in complex media (e.g., physiological fluids), are completely avoided, which can facilitate development of innovative colorimetric mechanoplasmonic bioanalytical assays and sensors that enables optical biodetection by means of mechanical stimuli.

2.5. Improving Signal-to-Noise Ratio

The 3D architecture of BC result in a high local concentration of AuNPs in the BC–AuNP composites and consequently a high absolute LSPR signal intensity, which facilitate sensitive detection of spectral changes. Whereas the mechanoplasmonic response was very distinct, LSPR shifts caused by the local RI changes caused by protein adsorption are much less pronounced (Figure S14, Supporting Information). However, the possibility to detect small refractometric changes in combination with high surface sensitivity make LSPR in general an attractive and widely used transduction method for RI-based biosensing.[8,48] Despite their rather low RI sensitivity (η < 100 nm per RIU)[38] spherical AuNPs are often used in biosensing applications because of their high figure of merit (FOM) defined as η divided by the resonance linewidth (full width at half maximum, FWHM).[49] In conventional LSPR-based refractometric biosensors, the AuNPs are typically immobilized on a 2D glass or polymer substrate.[50–52] For the BC–AuNP composite, the LSPR peak position was identical to AuNPs adsorbed to a conventional polymeric 2D surface but signal intensity was about a factor of 6 higher (**Figure 6**a). In contrast to a transparent glass/plastic substrate the BC is translucent, but since the BC membranes used were very thin (<0.5 mm), the effects of scattering on the sensitive was negligible but resulted in a slight blueshift ($\Delta\lambda_{max} \approx 1$ nm) of the LSPR band compared to AuNPs in suspension (Figure S4b,c, Supporting Information). The RI sensitivity of the immobilized AuNPs was very similar for the two substrates, 68 nm/RIU and 69 nm/RIU for the 2D surface and BC, respectively (Figure 6b). In addition, the FOM for the AuNPs immobilized on the 2D surface and in BC was identical, 1.2 RIU^{-1}, indicating that the BC–AuNP should be well suited also for RI sensing. In addition, the higher signal-to-noise ratio (S/N) of the BC–AuNP composite (≈450) as compared to the corresponding 2D substrate (≈250) can have a dramatic positive effect on sensor performance. Simulating the

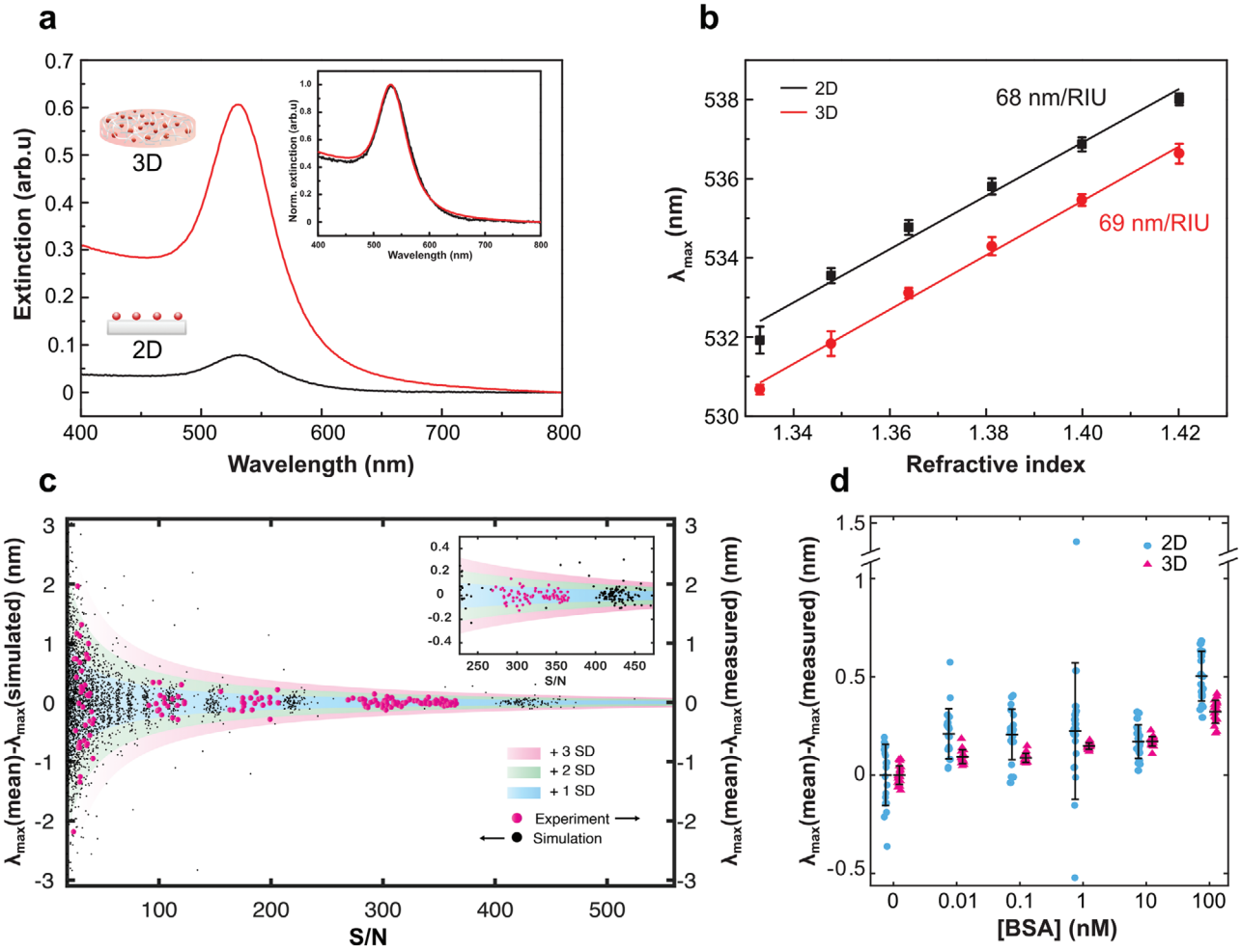

Figure 6. a) UV–vis spectra and b) corresponding refractive index sensitivity of AuNPs immobilized in BC (3D) and on a polymeric 2D substrate. Error bars show standard deviation. Inset in a) shows normalized UV–vis spectra of AuNPs in 3D (BC–AuNP) and 2D, respectively. c) Precision in LSPR peak determination as a function of signal-to-noise ratio as determined experimentally and by simulations. d) LSPR peak shift upon BSA adsorption to BC–AuNP (red) and AuNPs on a polymeric 2D substrate (blue). Error bars show standard deviations.

effects of increasing S/N on the accuracy in detecting the true LSPR peak position show that a sensor using the BC–AuNP composite should be able to discriminate a shift in the LSPR band that is about a factor of 2.3 smaller than when using a conventional 2D substrate (Figure 6c). These findings were experimental verified by acquiring 10 consecutive UV–vis spectra at different concentration of AuNPs (ø 50 nm) to achieve an estimate of the variation in the LSPR peak position at different S/N ratios (Figure 6c). The improvement in precision in the readout of the response upon BSA adsorption (Figure 6d) further shows that the BC–AuNP composite can outperform conventional 2D-LSPR biosensor configurations and facilitate development of novel BC–AuNP based sensor strategies. In addition, because of the intense color of the membranes, even relatively small LSPR shifts can be potentially visualized by the naked eye (Figure S14b,c, Supporting Information). This effect can likely be pronounced using nanoparticles with an LSPR band in a wavelength range better suited for visualization of color changes, which we have shown in previous work can enable detection of peak shifts as small as 2–3 nm.[53]

2.6. Nonlinear Optical Effects and Plasmonic Heating

The possibility to dynamically change the plasmonic properties of the BC–AuNP composites by applying pressure further enables exploration of nonlinear optical effects.[54] The redshift of the LSPR band upon compression of the BC–AuNP membranes enhances the absorption cross-section in the near-infrared (NIR) range. This in turn increases the probability of a sequential two-photon absorption process when illuminated using focused NIR light from femto-second-pulsed lasers, operating in the tissue transparent wavelength region.[55,56] The resulting multiphoton-induced luminescence (MIL) of the compressed BC–AuNP membranes could be clearly visualized in far-field multiphoton laser scanning microscopy (MPM) (**Figure 7**a,b and Figure S15, Supporting Information). In contrast, the noncompressed membranes showed no MIL signal (Figure 7a, inset). We have recently demonstrated that aggregation of spherical AuNPs in suspension results in MIL as a result of specific biorecognition,[55] but to our knowledge, a mechanically induced MIL signal has never previously been

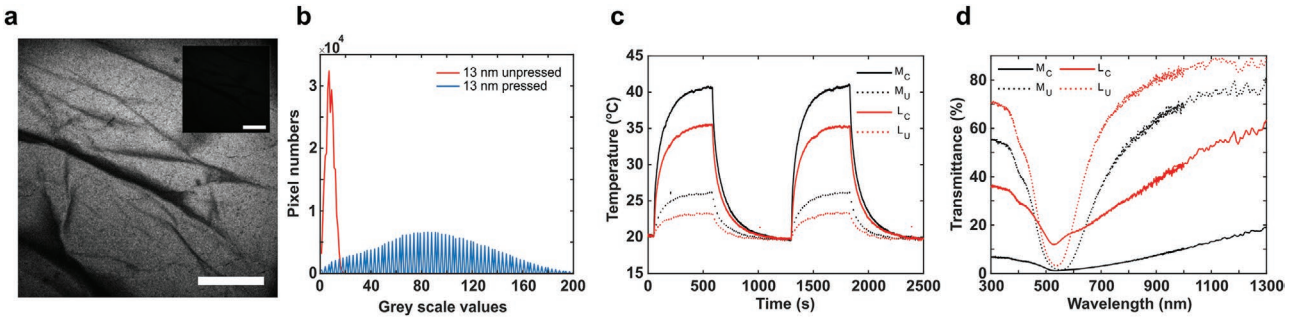

Figure 7. a) Far-field multiphoton laser scanning microscopy (MPM) image of BC–AuNP composite (AuNP ø 13 nm) after compression and before compression (inset), scale bars: 100 µm. b) MPM intensity distribution before (red) and after (blue) compression. c) Photothermal heating of compressed (C) and uncompressed (U) BC–AuNP composite with medium ($M_{C/U}$) and low ($L_{C/U}$) concentration of AuNPs, respectively, when exposed to laser light. d) Transmission spectroscopy of BC–AuNP composites mentioned in (c).

reported. Triggering nonlinear optical effects by mechanical stimuli represents a new possibility for modulating the optical properties of soft nanoplasmonic materials.

In addition, the large absorption cross section of AuNPs can result in significant heat generation when irradiated at the LSPR frequency as a result of electron–phonon and phonon–phonon processes.[57] A weak plasmonic heating in the uncompressed BC–AuNP composites was obtained by irradiation with NIR laser diodes showing emission in the first and second optical tissue windows (808 and 1064 nm), which slightly increased when increasing the concentration of the AuNPs (Figure 7c and Figure S16, Supporting Information). In contrast, compression of the BC–AuNP composites resulted in a large decrease in transmittance (Figure 7d) and a drastic increase in heat generation leading to a fourfold amplification of the light-induced temperature increment. The possibility to tune the plasmonic properties by mechanical stimuli can thus be utilized to enhance the thermoplasmonic performance of the BC–AuNP composites, which could be exploited to develop very efficient, biocompatible and highly stable implantable heat generators controlled by high penetration NIR light.

3. Conclusions

A novel and versatile method for fabrication of nanocomposites based on bacterial cellulose (BC) and metal NPs based on self-assembly is described. In contrast to methods relying on in situ synthesis, self-assembly enables the use of well-defined colloidal NPs of different sizes, shapes and composition, resulting in nanocomposites with distinct and tunable optical and biophysical properties, including mechanoplasmonic effects. Compression of BC–AuNP composites leads to controlled near-field coupling between the NPs, which is translated to large controlled spectral variations, including resonance redshifts and large increase in the absorption wavelength ranges. Importantly, the adsorption of biomolecules on the NPs can totally screen their near-field interaction upon compression, thereby offering a route for development of colorimetric mechanoplasmonic biosensors. The 3D structure of the BC–AuNP composites further provide a drastic increase in the signal-to-noise ratio of the spectral measurements. The mechanically induced broadening of the plasmonic absorption band can also be used to accurately amplify the optical properties of the materials, enabling new applications based on nonlinear optical effects and enhanced thermoplasmonic heat generation. The versatility of this self-assembly strategy, further demonstrated by generating antibacterial BC–AgNP composites, composites containing both AgNPs and AuNPs, as well as BC with anisotropic NPs, opens the path for BC–metal NP composites as multifunctional soft materials for emerging applications, spanning from wound care and biosensing to optics and electronics.

4. Experimental Section

General: BC produced from *Komagataeibacter xylinus* was obtained from S2Medical AB (Linköping, Sweden). The BC membranes were about 0.5 mm in thickness and 6 mm disks were cut out using a biopsy punch. All chemicals were obtained from Merck KGaA (Darmstadt, Germany) and used without further purification unless otherwise noted. AuNPs (ø 50 nm) and AgNPs (ø 40 nm) were obtained from BBI Solutions, (Crumlin, UK) and AgNPs (ø 20 nm) were obtained from Cline Scientific AB (Gothenburg, Sweden). Synthesis procedures for all other NPs are described in the Supporting Information.

NP Immobilization in BC: For immobilization of AuNPs and AgNPs, BC membranes were rinsed in MQ water and incubated from 12 h up to 30 d in an aqueous suspension of the NPs at RT on a rocking table. The concentration of AuNPs was varied between 60×10^{-12} M and 14.6×10^{-9} M, and the concentration of AgNPs was 3.75×10^{-12} M. The NaCl concentration was varied between 0.11×10^{-3} and 5×10^{-3} M. When coimmobilizing AuNPs (ø 50 nm) and AgNPs (ø 20 nm), AgNPs (0.77×10^{-9} M) and AuNPs (46×10^{-12} M) were mixed in varying ratios ([AgNP]:[AuNP]; 1:0.9; 1.9:1; 2.9:1; 4.2:1) and incubated for 7 d at RT on a rocking table followed by rinsing in MQ water. Extinction spectra of NP–BC composites were recorded using a microplate reader (Tecan Infinite M1000 Pro, Tecan Austria GmbH, Grödig/Salzburg, Austria). For adsorption kinetics experiments, a BC membrane was placed at the bottom of a cuvette and 1 mL AuNP (ø 50 nm) suspension (75×10^{-12} M, 5×10^{-3} M NaCl) was added on top. UV–vis spectra of the suspensions were measured at several time points with a benchtop UV–vis spectrophotometer (UV-2450, Shimadzu). Samples were kept on a rocking table between measurements. For refractive index sensitivity measurements and BSA adsorption measurements, BC membranes were placed in a 96-well microplate and 300 µL AuNP (ø 50 nm) suspension (60×10^{-12} M, 4×10^{-3} M NaCl) was added on top. Incubation time was 5 d after which the BC–AuNP composites were rinsed with MQ water. Adsorption of anisotropic NPs to BC was done by carefully heating a suspension of gold AuNR suspension (≈0.5 mL in an Eppendorf tube) until all CTAB crystals were dissolved. The suspension was then centrifuged at 8000 rpm for 6.5 min and the supernatant removed. The

NPs were then resuspended in 500 µL MQ water and a BC membrane was added to the tube. The sample was left on a rocking table and incubated for 48 h before being extracted from the suspension and rinsed with MQ water. Experimental details for analysis of optical and biophysical properties are available in Supporting Information.

Supporting Information

Supporting Information is available from the Wiley Online Library or from the author.

Acknowledgements

This work was supported by the Swedish Foundation for Strategic Research (SFF) grant no. FFL15-0026 and framework grant RMX18-0039 (HEALiX), the Swedish Government Strategic Research Area in Materials Science on Functional Materials at Linköping University (Faculty Grant SFO-Mat-LiU no. 2009-00971), the competence center FunMat-II that is financially supported by Vinnova (grant no. 2016-05156), and the Knut and Alice Wallenberg Foundation (grant no. KAW 2016.0231), the Swedish Research Council (grant Nos. 2017-05178 and 2015-05002) and the Spanish Ministerio de Ciencia, Innovación y Universidades (MICINN) through the MAT2016-77391-R. The ICN2 was supported by the Severo Ochoa Centres of Excellence programme, funded by the Spanish Research Agency (AEI, grant no. SEV-2017-0706). The authors thank Bela Nagy for input on modeling and S/N simulation and M. Magnusson at Linköping University for valuable input on signal theory.

Conflict of Interest

The authors declare no conflict of interest.

Keywords

antimicrobials, bacterial cellulose, gold nanoparticles, nanocomposite, sensors

Received: June 4, 2020
Revised: June 16, 2020
Published online: August 9, 2020

[1] L. Tian, J. Luan, K. K. Liu, Q. Jiang, S. Tadepalli, M. K. Gupta, R. R. Naik, S. Singamaneni, *Nano Lett.* **2016**, *16*, 609.
[2] E. Morales-Narváez, H. Golmohammadi, T. Naghdi, H. Yousefi, U. Kostiv, D. Horák, N. Pourreza, A. Merkoçi, *ACS Nano* **2015**, *9*, 7296.
[3] X. Du, Z. Zhang, W. Liu, Y. Deng, *Nano Energy* **2017**, *35*, 299.
[4] Z. Shi, G. O. Phillips, G. Yang, *Nanoscale* **2013**, *5*, 3194.
[5] M. Kaushik, A. Moores, *Green Chem.* **2016**, *18*, 622.
[6] M. Chen, H. Kang, Y. Gong, J. Guo, H. Zhang, R. Liu, *ACS Appl. Mater. Interfaces* **2015**, *7*, 21717.
[7] E. Lam, K. B. Male, J. H. Chong, A. C. W. Leung, J. H. T. Luong, *Trends Biotechnol.* **2012**, *30*, 283.
[8] Y. Chen, S. Han, S. Yang, Q. Pu, *Dyes Pigm.* **2017**, *142*, 126.
[9] D. Klemm, F. Kramer, S. Moritz, T. Lindström, M. Ankerfors, D. Gray, A. Dorris, *Angew. Chem., Int. Ed.* **2011**, *50*, 5438.
[10] A. J. Brown, *J. Chem. Soc., Trans.* **1886**, *49*, 432.
[11] U. Römling, M. Y. Galperin, *Trends Microbiol.* **2015**, *23*, 545.
[12] K.-Y. Lee, G. Buldum, A. Mantalaris, A. Bismarck, *Macromol. Biosci.* **2014**, *14*, 10.
[13] D. Klemm, D. Schumann, U. Udhardt, S. Marsch, *Prog. Polym. Sci.* **2001**, *26*, 1561.
[14] M. M. Rahman, A. N. Netravali, *ACS Macro Lett.* **2016**, *5*, 1070.
[15] R. Portela, C. R. Leal, P. L. Almeida, R. G. Sobral, *Microb. Biotechnol.* **2019**, *12*, 586.
[16] A. Svensson, E. Nicklasson, T. Harrah, B. Panilaitis, D. L. Kaplan, M. Brittberg, P. Gatenholm, *Biomaterials* **2005**, *26*, 419.
[17] J. Gutierrez, S. C. M. Fernandes, I. Mondragon, A. Tercjak, *ChemSusChem* **2012**, *5*, 2323.
[18] A. Aboelnaga, M. Elmasry, O. A. Adly, M. A. Elbadawy, A. H. Abbas, I. Abdelrahman, O. Salah, I. Steinvall, *Burns* **2018**, *44*, 1982.
[19] T. Sivlér, P. Sivlér, M. Skog, L. Conti, D. Aili, *Adv. Skin Wound Care* **2018**, *31*, 306.
[20] T. Maneerung, S. Tokura, R. Rujiravanit, *Carbohydr. Polym.* **2008**, *72*, 43.
[21] J. He, T. Kunitake, A. Nakao, *Chem. Mater.* **2003**, *15*, 4401.
[22] T. Zhang, W. Wang, D. Zhang, X. Zhang, M. Yurong, Y. Zhou, L. Qi, *Adv. Funct. Mater.* **2010**, *20*, 1152.
[23] L. C. de Santa Maria, A. L. C. Santos, P. C. Oliveira, H. S. Barud, Y. Messaddeq, S. J. L. Ribeiro, *Mater. Lett.* **2009**, *63*, 797.
[24] H. S. Barud, T. Regiani, R. F. C. Marques, W. R. Lustri, Y. Messaddeq, S. J. L. Ribeiro, *J. Nanomater.* **2011**, *2011*, 721631.
[25] S. Roig-Sanchez, E. Jungstedt, I. Anton-Sales, D. C. Malaspina, J. Faraudo, L. A. Berglund, A. Laromaine, A. Roig, *Nanoscale Horiz.* **2019**, *4*, 634.
[26] S. Pal, R. Nisi, M. Stoppa, A. Licciulli, *ACS Omega* **2017**, *2*, 3632.
[27] S. Gea, C. T. Reynolds, N. Roohpour, B. Wirjosentono, N. Soykeabkaew, E. Bilotti, T. Peijs, *Bioresour. Technol.* **2011**, *102*, 9105.
[28] L. Francisco-Aldana, E. Morales-Narváez, *J. Phys.: Photonics* **2019**, *1*, 04LT01.
[29] N. G. Bastús, J. Comenge, V. Puntes, *Langmuir* **2011**, *27*, 11098.
[30] M. R. Langille, M. L. Personick, J. Zhang, C. A. Mirkin, *J. Am. Chem. Soc.* **2012**, *134*, 14542.
[31] M. L. Personick, C. A. Mirkin, *J. Am. Chem. Soc.* **2013**, *135*, 18238.
[32] M. M. Shahjamali, M. Bosman, S. Cao, X. Huang, S. Saadat, E. Martinsson, D. Aili, Y. Y. Tay, B. Liedberg, S. C. J. Loo, H. Zhang, F. Boey, C. Xue, *Adv. Funct. Mater.* **2012**, *22*, 849.
[33] C. Daruich De Souza, B. Ribeiro Nogueira, M. E. C. M. Rostelato, *J. Alloys Compd.* **2019**, *798*, 714.
[34] I. Pastoriza-Santos, C. Kinnear, J. Pérez-Juste, P. Mulvaney, L. M. Liz-Marzán, *Nat. Rev. Mater.* **2018**, *3*, 375.
[35] Y. Li, Y. Tian, W. Zheng, Y. Feng, R. Huang, J. Shao, R. Tang, P. Wang, Y. Jia, J. Zhang, W. Zheng, G. Yang, X. Jiang, *Small* **2017**, *13*, 1700130.
[36] Y. Wang, D. Aili, R. Selegård, Y. Tay, L. Baltzer, H. Zhang, B. Liedberg, *J. Mater. Chem.* **2012**, *22*, 20368.
[37] A. M. Sokolnicki, R. J. Fisher, T. P. Harrah, D. L. Kaplan, *J. Membr. Sci.* **2006**, *272*, 15.
[38] E. Martinsson, B. Sepulveda, P. Chen, A. Elfwing, B. Liedberg, D. Aili, *Plasmonics* **2014**, *9*, 773.
[39] E. Martinsson, M. A. Otte, M. M. Shahjamali, B. Sepulveda, D. Aili, *J. Phys. Chem. C* **2014**, *118*, 24680.
[40] D. Aili, P. Gryko, B. Sepulveda, J. A. G. Dick, N. Kirby, R. Heenan, L. Baltzer, B. Liedberg, M. P. Ryan, M. M. Stevens, *Nano Lett.* **2011**, *11*, 5564.
[41] D. F. Evans, H. Wennerström, *The Colloidal Domain: Where Physics, Chemistry, Biology, and Technology Meet*, 2nd ed., John Wiley & Sons, Ltd, New York **1999**.
[42] H. A. Kramers, *Physica* **1940**, *7*, 284.
[43] J. Wu, Y. Zheng, X. Wen, Q. Lin, X. Chen, Z. Wu, *Biomed. Mater.* **2014**, *9*, 035005.
[44] Z. M. Xiu, J. Ma, P. J. J. Alvarez, *Environ. Sci. Technol.* **2011**, *45*, 9003.

[45] C. Andrésen, S. Jalal, D. Aili, Y. Wang, S. Islam, A. Jarl, B. Liedberg, B. Wretlind, L.-G. Mårtensson, M. Sunnerhagen, *Protein Sci.* **2010**, *19*, 680.
[46] M. Park, H. Chang, D. H. Jeong, J. Hyun, *BioChip J.* **2013**, *7*, 234.
[47] D. Aili, R. Selegård, L. Baltzer, K. Enander, B. Liedberg, *Small* **2009**, *5*, 2445.
[48] Y.-J. Lai, W.-L. Tseng, *Analyst* **2011**, *136*, 2712.
[49] L. J. Sherry, R. Jin, C. A. Mirkin, G. C. Schatz, R. P. Van Duyne, *Nano Lett.* **2006**, *6*, 2060.
[50] C. Xue, Z. Li, C. A. Mirkin, *Small* **2005**, *1*, 513.
[51] X. Y. Zhang, A. Hu, T. Zhang, W. Lei, X. J. Xue, Y. Zhou, W. W. Duley, *ACS Nano* **2011**, *5*, 9082.
[52] N. Nath, A. Chilkoti, *Anal. Chem.* **2004**, *76*, 5370.
[53] P. Chen, X. Liu, G. Goyal, N. T. Tran, J. C. Shing Ho, Y. Wang, D. Aili, B. Liedberg, *Anal. Chem.* **2018**, *90*, 4916.
[54] M. Kauranen, A. V Zayats, *Nat. Photonics* **2012**, *6*, 737.
[55] J. Borglin, R. Selegård, D. Aili, M. B. Ericson, *Nano Lett.* **2017**, *17*, 2102.
[56] J. Borglin, S. Guldbrand, H. Evenbratt, V. Kirejev, H. Grönbeck, M. B. Ericson, *Appl. Phys. Lett.* **2015**, *107*, 234101.
[57] S. Link, M. A. El-Sayed, *Int. Rev. Phys. Chem.* **2000**, *19*, 409.